

# Learning two-phase microstructure evolution using neural operators and autoencoder architectures

Vivek Oommen, Khemraj Shukla, Somdatta Goswami, Rémi Dingreville, and George Em Karniadakis

---

## Abstract

Phase-field modeling is an effective mesoscale method for capturing the evolution dynamics of materials, e.g., in spinodal decomposition of a two-phase mixture. However, the accuracy of high-fidelity phase field models comes at a substantial computational cost. Hence, fast and generalizable surrogate models are needed to alleviate the cost in computationally taxing processes such as in optimization and design of materials. The intrinsic discontinuous nature of the physical phenomena incurred by the presence of sharp phase boundaries makes the training of the surrogate model cumbersome. We develop a new framework that integrates a convolutional autoencoder architecture with a deep neural operator (DeepONet) to learn the dynamic evolution of a two-phase mixture. We utilize the convolutional autoencoder to provide a compact representation of the microstructure data in a low-dimensional latent space. DeepONet, which consists of two sub-networks, one for encoding the input function at a fixed number of sensors locations (branch net) and another for encoding the locations for the output functions (trunk net), learns the mesoscale dynamics of the microstructure evolution in the latent space. The decoder part of the convolutional autoencoder can then reconstruct the time-evolved microstructure from the DeepONet predictions. The result is an efficient and accurate accelerated phase-field framework that outperforms other neural-network-based approaches while at the same time being robust to noisy inputs.

*Keywords:* Phase-field method, DeepONet, convolutional autoencoder, transposed convolutional decoder, Surrogate modeling, neural operator

---

## 1. Introduction

The phase-field approach has emerged as a powerful heuristic tool for modeling and predicting mesoscale microstructural evolution in a wide variety of material processes [1–5]. This method models interfacial dynamics without the overhead of resorting to advanced interfacial tracking algorithms such as level-set [6] or adaptive meshing [7]. Scalar, auxiliary, continuous field variables (so called phase-field variables) are used to represent the state of the microstructure dynamics via the smooth variation across the interfaces such as in crack growth and propagation [8, 9], thin-film deposition [10, 11], and dislocation dynamics [12] to name a few. The Cahn-Hilliard, nonlinear diffusion equation [1, 13, 14], is one of the most commonly used governing equations in phase-field models. It describes the process of phase separation, by which a two-phase mixture spontaneously separates and form domains pure in each component. The Cahn-Hilliard

equation finds applications in diverse fields ranging from complex fluids to soft matter and serves as the starting of many phase-field models for microstructure evolution.

Traditional numerical approaches to solve the fourth-order parabolic Cahn–Hilliard equation include finite differences [15], spectral approximation [16], finite element analysis with mixed methods [17], and isogeometric analysis [18, 19] to name a few. The coupled stiff equation simultaneously captures a quick phase separation and a very slow coalescence. Evidently, the two sub-processes operate on significantly different spatial and temporal scales, which makes it challenging to solve efficiently and accurately within realistic time constraints and reasonable computational capabilities [20]. Improvements in computational complexity have been enabled by the growing interest in data-driven models using machine learning (ML) methods. However, striking a balance between computational efficiency and accuracy has often been a challenge while employing these methods. To give an example, on one side, for complex and multi-variate phase-field models, the efficient Green’s function [21] does not ensure an accurate solution, while on the other side Bayesian optimization [22, 23] techniques solve such coupled models but at a higher computational cost.

Modern ML models have paved the way for the development of fast emulators for solving parametric partial differential equations (PDEs) [24–31]. A new generation of strategies for accelerating the simulation of PDEs is emerging. A promising approach for accelerating the prediction of the phase field-based microstructure evolution [32, 33] consists of using recurrent neural networks (RNNs) to learn the time-dependent, microstructure evolution in latent space. Within this framework statistical functions combined with linear and nonlinear embedding techniques are used to represent the microstructure evolution in latent space. The RNN-based surrogate model demonstrated success in generating rapid predictions of the microstructure evolution in a low-dimensional space of the autocorrelations. The microstructure reconstructed from the statistical functions using for instance a phase recovery algorithm [34] is used as an input for a high-fidelity solver that marches ahead in time. The developed approach reported 5% loss in accuracy against the high-fidelity phase-field solvers. However, the developed model also comes with certain potential challenges. First, the training and inference using RNNs as a surrogate model [32] can be relatively slow due to the temporal dependence of the current predicted field on fields predicted at previous time steps, prohibiting efficiency of algorithm for large datasets. Second, the RNN-based architecture learns the underlying evolution dynamics in terms of statistical functions (non-primitive variables) of the microstructure. Reconstructing a microstructure from these statistical functions is a non-trivial and ill-posed problem [35]. This reconstruction step can incur additional errors especially for interfacial dynamics problems where resolving intricate spatial length scales such as in dendrite growth phase-field problems is key.

In this work, we propose an alternative approach to circumvent these challenges. We can formulate the microstructure evolution problem as being equivalent to learning a mapping function  $\mathcal{G} : \mathbf{u} \rightarrow \mathbf{f}$  such that,

$$\mathcal{G}(\mathbf{u}(x, y, t)) = \mathbf{f}(x, y, t), \quad (1)$$

where  $\mathbf{u}$  is the history of microstructure evolution and  $\mathbf{f}(x, y, t)$  is the state of the microstructure at time  $t$ .

We utilize a convolutional autoencoder to provide a compact representation of the

microstructure data in a low-dimensional latent space.

This convolutional autoencoder approach is then combined with a Deep Operator Network [36] (DeepONet) to learn the dynamics of two-phase microstructures in the autoencoder latent space. The decoder part of the convolutional autoencoder can then reconstruct the time-evolved microstructure from the the DeepONet predictions. The DeepONet architecture has demonstrated its ability to model the governing differential equations (ODEs and PDEs) of the problem by learning the underlying operator, a mapping from functions to functions, from the available datasets for broad range of problems [27, 37].

Figure 1 illustrates the complete end-to-end workflow of the proposed algorithm. Specifically, in Section 2 we present the phase-field model and the procedures to train both the convolutional autoencoder and the DeepONet. We demonstrate the performance of this accelerated framework in terms of its predictability, computational efficiency, and robustness to noise in Section 3.

## 2. Methodology

### 2.1. Phase-field model of the spinodal decomposition of a two-phase mixture

We illustrate our accelerated phase-field workflow on the simplest case of the spinodal decomposition of a two-phase mixture. This model is highly relevant to many phase-field models. In the spinodal decomposition of a two-phase mixture uses a single order parameter,  $\phi(\mathbf{x}, t)$  to describe the atomic fraction of solute diffusing within a matrix. The free energy of the system is expressed by the Cahn-Hilliard equation based on the Onsager force-flux relationship such that

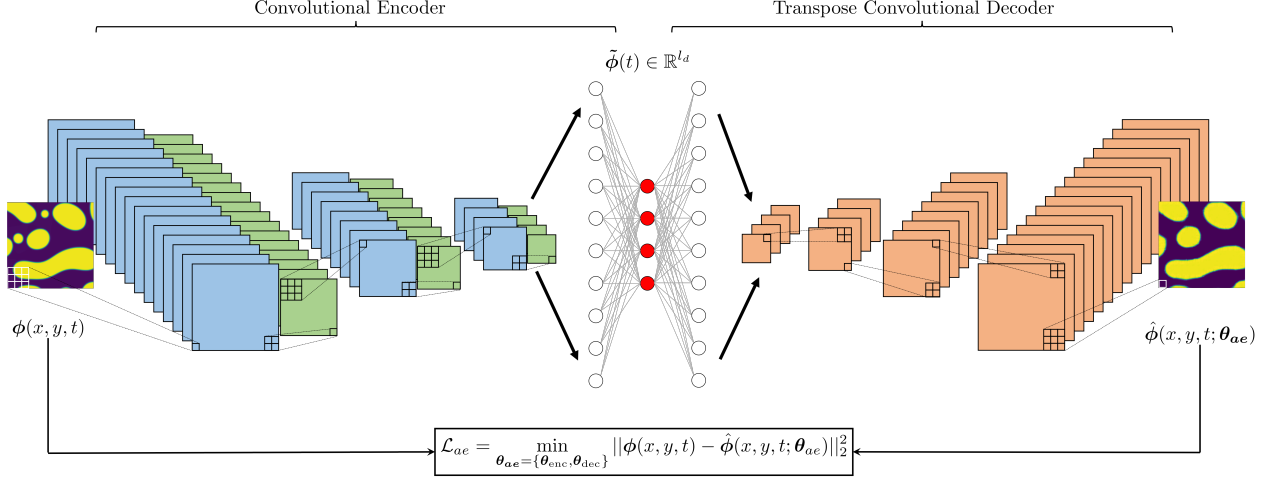
$$\frac{\partial \phi}{\partial t} = \nabla \cdot (M_c(\phi) \nabla [\omega_c(\phi^3 - \phi) + \kappa_c \nabla^2 \phi]), \quad (2)$$

$\omega_c$  is the height of the energy barrier between the two phases,  $\kappa_c$  is the gradient energy coefficient, and  $M_c$  denotes the concentration dependent mobility, with  $M_c = s(\phi)M_A + (1 - s(\phi))M_B$ . The function  $s$  defines a smooth interpolation to switch from phase ‘A’ to phase ‘B’. This interpolation function is defined as  $s(\phi) = \frac{1}{4}(2 - \phi)(1 + \phi)^2$ . In the present model, both the mobility and the interfacial energy are taken to be isotropic and  $\omega_c$  and  $\kappa_c$  are set to unity for simplicity. The evolution of one phase is expressed as a symmetric double-well potential, with minima at  $\phi \pm 1$ .

### 2.2. Microstructure-evolution dataset

The phase-field model described above is implemented using Sandia’s in-house multi-physics phase-field modeling code MEMPHIS [10, 38]. In order to generate a diverse and large set of simulation results exhibiting a rich variety of microstructure features, we independently sampled the phase fraction  $\phi_A$ , such that each phase has at least a minimum concentration of 0.15 (note that  $\phi_B = 1 - \phi_A$ ), and the phase mobilities  $M_A$  and  $M_B$  of species ‘A’ and ‘B’. Phase mobilities are sampled independently to vary in the range [0.01, 100]. In total we generated 500 triplets  $(\phi_A, M_A, M_B)$  using Latin Hypercube Sampling. All the simulations were performed using a two-dimensional (2D) square domain  $\Omega = [0, 1] \times [0, 1]$ , discretized with  $512 \times 512$  grid points, with a dimensionless spatial discretization of unity on either

### Step 1: Training Convolutional Autoencoder



### Step 2: Training DeepONet in latent space

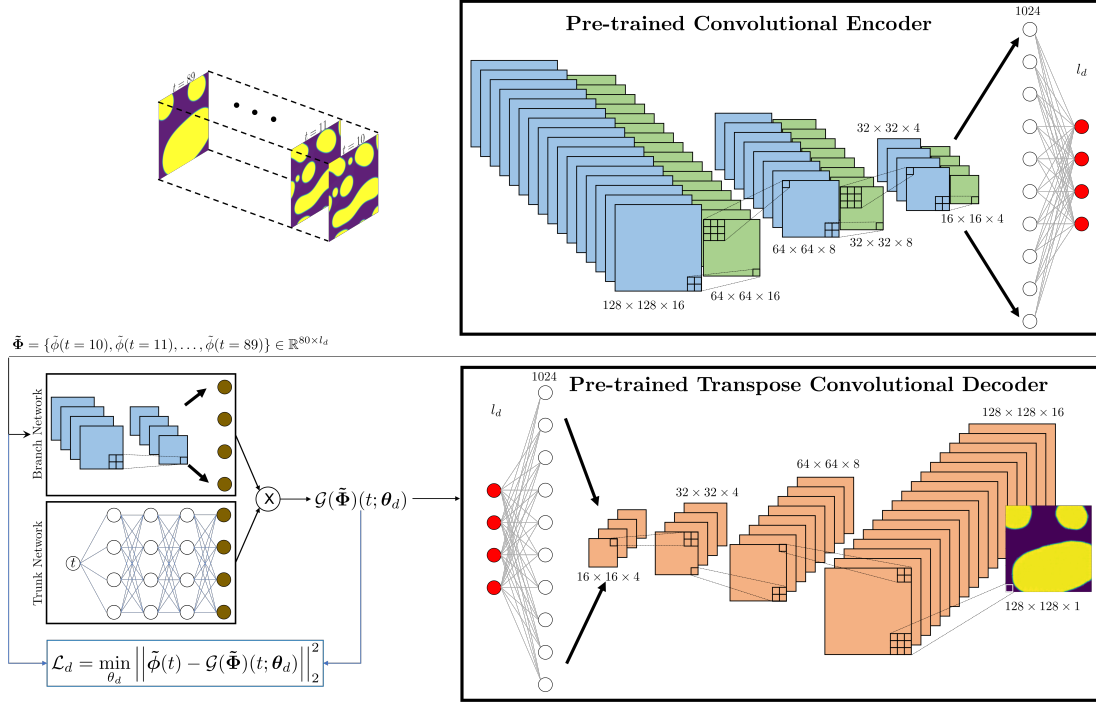


Figure 1: Schematic representation of DeepONet with convolutional autoencoder. Step 1 involves training of the convolutional autoencoder to minimize  $\mathcal{L}_{ae}$ . The encoder learns a suitable transformation from the high-dimensional microstructure to a low-dimensional latent space through a series of convolution (blue layers) and MaxPooling (green layers) operations. The decoder remaps the latent microstructure back to the original space by performing transpose convolution (orange layers) operations. Detailed description of the architecture is provided in Table 1. In step 2, we train the DeepONet in the latent space to minimize  $\mathcal{L}_d$ . The entire history of 80 steps is encoded by the pre-trained convolutional encoder as  $\tilde{\Phi}$ . DeepONet learns to predict  $\tilde{\phi}(t)$  at any desired time  $t$ , fed to the trunk network. The latent microstructure predicted by DeepONet is then re-mapped back to the primitive space by the transpose convolutional decoder.



direction, and a temporal differencing of  $1 \times 10^{-4}$ . The simulation domain's composition field is initialized using truncated random Gaussian distribution in the range  $[-1, 1]$  with  $\mu = \phi_A$ , and  $\sigma = 0.35$ . The microstructure was allowed to evolve and grow for 50,000,000 time steps, saving the state of the microstructural domain every 500,000 time steps, hence a total of 100 time frames were saved from each simulated case.

In order to use the data in the proposed algorithm, we downsampled each snapshot of our  $512 \times 512$  domain into four images of  $256 \times 256$ , and later used cubic interpolation [39] to further reduce the resolution to  $128 \times 128$ . Hence, from the 500 microstructure evolution samples, we were able to generate 2000 microstructure evolution samples of  $128 \times 128$  resolution. From this dataset, we have used 1600 cases for training the DeepONet and 400 cases for testing the network accuracy. Since the compositional field is randomly distributed spatially, the microstructure has no recognizable features at the first frame  $t_0$ . The quick development of subdomains is then observed between frames  $t_0$  and  $t_{10}$ , followed by a smooth and steady coalescence and growth of the microstructure from time frames  $t_{10}$  to  $t_{100}$ . We have trained our proposed model based on this observation starting at time frame,  $t_{10}$ , when the microstructure had reached a slow and steady development regime.

### 2.3. Training the autoencoder: Learning the latent microstructure representation

In this work, each microstructure evolution is represented by  $(N_T, N_x, N_y) = (80 \times 128 \times 128)$ , with  $N_T$  representing the number of snapshots and  $N_x \times N_y$  denoting the the spatial resolution along  $x$ - and  $y$ - direction, respectively. To handle the entire feature space ( $\mathbb{R}^{128 \times 128}$ ) 16,384 distinct features are required to represent the microstructure at each time step. Subsequently, to compute the prediction for all 1600 microstructure evolutions, we will have  $1600 \times 80 \times 16384$  ( $\approx 2.5$  Billion) 32-bit floating data points. Learning microstructure dynamics from such a high-dimensional dataset is challenging.

To circumvent issues pertaining to the data dimensionality and preparing the phase-field microstructure data for DeepONet training, we explored a couple of options. First, we tried using Principal Component Analysis (PCA) with linear kernel, for reducing the dimensionality of the data [21, 40, 41]. The low-dimensional representation of the data obtained from PCA is a linear transformation of the high-dimensional data and discards the insignificant modes (eigen/singular) corresponding to the lower eigen/singular values ( $\lambda_i$ ). However, the system considered here is not diffusive and this is shown in Fig. 2. Therefore, using PCA for reducing the dimensionality of the microstructure description could result in the loss of valuable information, if only a convenient low number of principal components are considered. Learning a non-linear mapping from a high dimensional to a low-dimensional latent space is one way to compress data without losing as much information as in the PCA. An autoencoder precisely does this by learning a non-linear transformation to a low dimensional latent space using an encoder. The decoder learns the mapping to retrieve initial high dimensional data from its latent representation.

In this study, we have used a convolutional autoencoder [42] with convolutional layers in the encoder and transpose convolutional layers in the decoder as shown in Fig. 1. The encoder learns a nonlinear mapping of the high-dimensional microstructure data,  $\phi(\mathbf{x}, \mathbf{y}, t)$ , to a low-dimensional latent space represented by  $\tilde{\phi}(t)$  and is expressed as

$$\alpha_{\theta_{\text{enc}}} : \phi(\mathbf{x}, \mathbf{y}, t) \rightarrow \tilde{\phi}(t), \quad (3a)$$

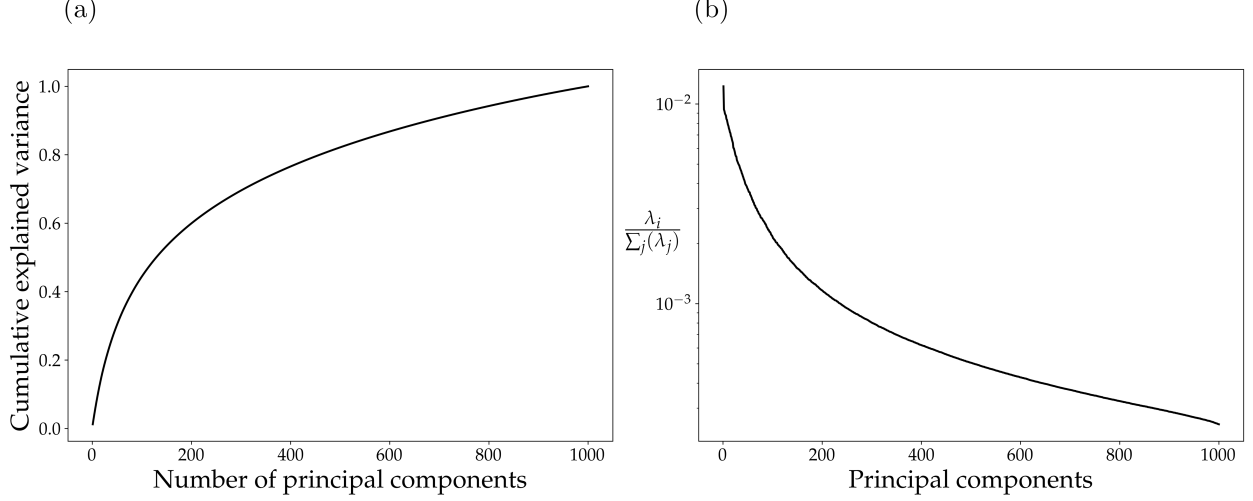


Figure 2: (a) The cumulative explained variance curve on the dominant 1000 eigenvalues of the phase-field microstructure (b) The energy curve on the dominant 1000 eigenvalues of the phase-field microstructure. The two plots suggest that microstructure data represent a non-diffusive system.

$$\beta_{\theta_{\text{dec}}} : \tilde{\phi}(t) \rightarrow \hat{\phi}(\mathbf{x}, \mathbf{y}, t), \quad (3b)$$

where  $\alpha$  and  $\beta$  represent the mappings performed by the encoder and the decoder, respectively. In Eq. (3a), the encoder takes  $\phi(\mathbf{x}, \mathbf{y}, t) \in \mathbb{R}^{128 \times 128}$  as input, and maps it to  $\tilde{\phi}(t) \in \mathbb{R}^{l_d}$ , where  $l_d$  is the dimension of the latent space.  $\theta_{\text{enc}}$  represents the trainable parameters of the convolutional encoder. Equation (3b) represents the decoder network, which takes the latent dimensional representation,  $\tilde{\phi}(t) \in \mathbb{R}^{l_d}$  as the input and predicts the primitive microstructure,  $\hat{\phi}(\mathbf{x}, \mathbf{y}, t) \in \mathbb{R}^{128 \times 128}$ , using transpose convolutional operations. The details of the autoencoder architecture are provided in Table 1.

$\theta_{\text{ae}}$  represents the trainable parameters of the autoencoder. These parameters are learned by minimizing the loss function,  $\mathcal{L}_{\text{ae}}$ , which reads

$$\mathcal{L}_{\text{ae}} = \min_{\theta_{\text{ae}} = \{\theta_{\text{enc}}, \theta_{\text{dec}}\}} \|\phi(\mathbf{x}, \mathbf{y}, t) - \hat{\phi}(\mathbf{x}, \mathbf{y}, t; \theta_{\text{ae}})\|_2^2 \quad (4)$$

Alternatively, the autoencoder provides a low-dimensional representation of the microstructure by learning a non-linear transformation to a latent space with  $l_d$  features. We also observe that it is easier to learn the microstructure dynamics in the latent space representation, learned by the autoencoder, than the original primitive form of the microstructure in real space. This is due to the presence of several high gradient regions in the original form of the microstructure as shown in Fig. 10(a). These high gradient regions in the solution are due to the nature of the governing Cahn-Hilliard equation. The latent microstructure representation in Fig. 10(b) is smoother and does not have high gradient regions. The latent representation of the data offers higher regularity and therefore, we achieve faster convergence during the training of the surrogate neural network model.

#### 2.4. Training the DeepONet: Learning the microstructure dynamics in lower dimensions

Neural operators generate nonlinear mappings across infinite dimensional function spaces on bounded domains, giving a novel simulation framework for multidimensional complex

Table 1: Details of the hyperparameters used in the convolutional autoencoder.

	Layer	Kernel Size	Width	Activation	Output
1	Conv2D	$3 \times 3$	16	ReLU	$128 \times 128 \times 16$
2	Max-Pool	$2 \times 2$			$64 \times 64 \times 16$
3	Conv2D	$3 \times 3$	8	ReLU	$64 \times 64 \times 8$
4	Max-Pool	$2 \times 2$			$32 \times 32 \times 8$
5	Conv2D	$3 \times 3$	4	ReLU	$32 \times 32 \times 4$
6	Max-Pool	$2 \times 2$			Reshaped to 1024
7	Fully connected		$l_d$	Linear	$l_d$
8	Fully connected		1024	ReLU	Reshaped to $16 \times 16 \times 4$
9	Transpose Conv2D	$2 \times 2$		ReLU	$32 \times 32 \times 4$
10	Transpose Conv2D	$2 \times 2$		ReLU	$64 \times 64 \times 8$
11	Transpose Conv2D	$2 \times 2$		ReLU	$128 \times 128 \times 16$
12	Transpose Conv2D	$3 \times 3$		ReLU	$128 \times 128 \times 1$

$l_d$  : dimension of latent space

dynamics prediction in real time. Once properly trained, such models are discretization invariant, which means they share the same network parameters regardless of how the underlying functional data is parameterized. DeepONet, originally proposed in [36], allows the mapping between infinite dimensional functions using deep neural networks. In this section, we provide a detailed description of the training of DeepONet to model the evolution of the microstructure in the latent dimension.

The unstacked DeepONet architecture is made up of two concurrent deep neural networks: one encodes the input function at fixed sensor locations (branch network), while the other represents the domain of the output function (trunk network). Time,  $t \in \mathbb{R}^1$ , is given as input to the trunk network while  $\tilde{\Phi} = \{\tilde{\phi}(t=10), \tilde{\phi}(t=11), \dots, \tilde{\phi}(t=89)\} \in \mathbb{R}^{80 \times l_d}$  is the input fed to the branch network.  $\tilde{\Phi}$  represents the phase field in the latent dimension,  $l_d$ , for all the 80 time steps available in the given dataset. The goal of the DeepONet is to learn the solution operator,  $\tilde{\phi}(t) \approx \hat{\phi}(t) = \mathcal{G}(\tilde{\Phi})(t)$  from the 1600 microstructure evolutions provided in the training dataset. The output of the DeepONet is a vector  $\in \mathbb{R}^{l_d}$  and is expressed as  $\mathcal{G}(\tilde{\Phi})(t; \theta_d)$ , where  $\theta_d = \{\mathbf{W}_d, \mathbf{b}_d\}$  includes the trainable weights,  $\mathbf{W}_d$ , and biases,  $\mathbf{b}_d$ , of the DeepONet model. The framework of the DeepONet allows the branch network to have a flexible architecture. To model the microstructure evolution, we have considered a fully-connected neural network for the trunk network. Due to the high-dimensional nature of the branch network input,  $\mathbb{R}^{80 \times l_d}$ , a convolutional neural network is used as the branch network because it utilizes the same kernels across time axis and enables the branch network to encode the entire history in a memory efficient manner. Hence, the input has to be reshaped to  $\mathbb{R}^{80 \times \sqrt{l_d} \times \sqrt{l_d}}$  before feeding it to the branch network. The network architecture is presented in Fig. 1. The trainable parameters of the DeepONet,  $\theta_d$ , are obtained by

minimizing a loss function,  $\mathcal{L}_d$ , defined as:

$$\mathcal{L}_d = \min_{\theta_d} \left\| \tilde{\phi}(t) - \mathcal{G}(\tilde{\Phi})(t; \theta_d) \right\|_2^2, \quad (5)$$

where  $\tilde{\phi}(t)$  is the ground truth for the low-dimensional phase field representation at time,  $t$  obtained from the convolutional encoder. The trained DeepONet is used to predict  $\tilde{\phi}(t) \in \mathbb{R}^{l_d}$ . The output of the DeepONet is fed into the transposed convolutional decoder to predict,  $\hat{\phi}(t) \in \mathbb{R}^{128 \times 128}$ .

The DeepONet is trained using the Adam optimizer [43]. The implementation has been carried out using the TensorFlow framework [44]. We use Xavier Initialization [45] to initialize the weights of all the models. The  $L^2$  norm of relative error,  $\mathcal{D}$ , is used as the evaluation metric to analyze the performance of each model considered in this study.  $\mathcal{D}$  is defined as:

$$\mathcal{D} = \frac{\sum_n \sum_x \sum_y \sum_t \left( \phi^{(n)}(x, y, t) - \hat{\phi}^{(n)}(x, y, t; \theta) \right)^2}{\sum_n \sum_x \sum_y \sum_t \phi^{(n)}(x, y, t)^2}, \quad (6)$$

where  $n$  corresponds to the  $n^{th}$  sample of the given dataset.

### 3. Results

#### 3.1. Training and optimization: impact of the size of latent space, $l_d$ , and DeepONet architecture

We first investigate the impact of the size of the latent dimension of the autoencoder,  $l_d$ , on model performance. To that effect, we trained 5 autoencoder models with  $l_d = 9, 25, 64, 100$ , and 196 respectively. Each autoencoder training took approximately 33 hours on one NVIDIA GeForce RTX 3090 GPU. Next, we trained the DeepONet model for 120000 epochs on the latent space learnt by the convolutional encoder of each of the 5 trained autoencoder models. The output of the DeepONet model is then sent to the trained convolutional decoder which performs a mapping from the latent space back to the original microstructure space,  $\hat{\phi}(x, y, t)$ . We evaluated each of the models on the basis of the relative  $L^2$  norm computed across the train and test dataset for all the time steps, including the forecasting timesteps,  $t = 90, \dots, 99$ . All the details of this survey analysis, including the DeepONet architecture, the  $L^2$  norm of relative error on train and test datasets, time taken for training the DeepONet model are reported in Table 2. The last layer of the branch and trunk networks for all the models uses a linear activation function.

From this comprehensive survey, we observe that the model predictions improve when increasing the size of the latent dimension. In general, DeepONet models with tanh and sin activation functions perform better compared to models with ReLU activation for this particular class of problems. Our best model consists of convolutional autoencoder with  $l_d = 196$  and a DeepONet model with architecture 1 and sin activation function. Although the training dataset consists of 1600 different microstructure-evolution trajectories, each represented by 80 snapshots from  $t = \{10, 11, \dots, 89\}$ , the DeepONet training is faster compared to the popular recurrent neural network architectures such as LSTMs or GRUs. Since DeepONet does not have recurrent connections, there are no temporal dependencies

Table 2: Detailed survey of different latent dimension size,  $l_d$ , network architecture, and non-linear activation functions.

$l_d$	DeepONet Architecture	Activation	$\mathcal{D}_{train}$	$\mathcal{D}_{test}$	DeepONet training time per 1000 epochs (s)
196	architecture 1	ReLU	0.03621	0.06803	56
		tanh	0.02177	0.06233	56
		sin	0.01408	0.01620	57
100	architecture 2	ReLU	0.04076	0.05991	31
		tanh	0.03196	0.04699	30
		sin	0.02684	0.03679	31
64	architecture 3	ReLU	0.06708	0.07791	31
		tanh	0.04773	0.06013	35
		sin	0.04781	0.05739	32
25	architecture 4	ReLU	0.16527	0.20097	19
		tanh	0.16507	0.20134	19
		sin	0.16551	0.20167	20
9	architecture 5	ReLU	0.31536	0.3186	10
		tanh	0.31523	0.31903	11
		sin	0.31539	0.31876	11

architecture	Branch Network	Trunk Network
1	$3 \times [\text{conv}(32, (3, 3))] + [1960]$	$2 \times [100] + [1960]$
2	$2 \times [\text{conv}(32, (3, 3))] + [1100]$	$2 \times [100] + [1100]$
3	$2 \times [\text{conv}(32, (3, 3))] + [512]$	$2 \times [100] + [512]$
4	$1 \times [\text{conv}(64, (3, 3))] + [500]$	$2 \times [100] + [500]$
5	$1 \times [\text{conv}(128, (3, 3))] + [180]$	$2 \times [100] + [180]$

during the training or at the inferring stage. Instead, for these temporal dependencies, we rely on the convolution operations that encodes information about the history through the branch network.

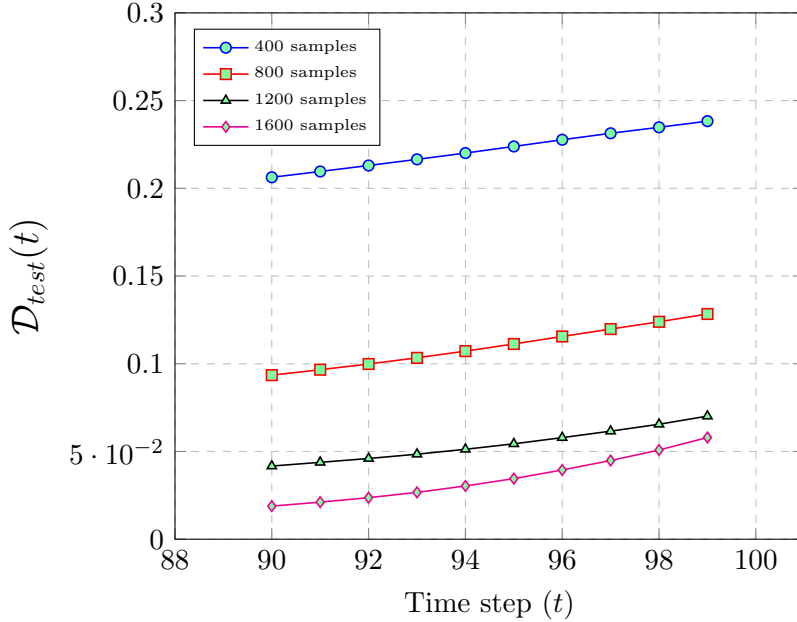


Figure 3: Sensitivity of the proposed surrogate model to the number samples in training data.  $\mathcal{D}_{test}(t)$ : represents  $\mathcal{D}(t)$  computed on test dataset as defined by Equation (7). We analyze the performance of each model on the basis of  $\mathcal{D}_{test}(t)$  at forecasting time steps.

We carried out a additional simulations to analyze the sensitivity of the proposed approach to the number of samples used for training. We consider training datasets with 25%, 50%, 75% and all the 1600 training samples. We adopted the same methodology proposed in Section 2 and trained separate Autoencoder-DeepONet models on each of these datasets. The model performance is evaluated on the basis of forecasting errors on test data, shown in Fig. 3.

As expected, we observe better accuracy in model’s predictions while increasing the number of training samples. The model trained with 1200 data samples shows similar accuracy as the best model trained with 1600 data samples.

Finally, we investigated the effect of using different loss functions on training of the autoencoder models. Specifically, we trained autoencoders by minimizing (1)  $L^1$  loss, (2) relative  $L^1$  loss, (3)  $L^2$  loss, (4) relative  $L^2$  loss, and (5) mixed loss ( $L^2$  loss for the initial 5000 epochs and  $L^1$  loss for the remaining epochs). Now, (i) we train DeepONet model with architecture 1 (Table 2) on each of the learned latent microstructure data and (ii) re-transform the DeepONet predictions using pre-trained decoder to retrieve the microstructure. Finally, we analyzed the model performance by computing the forecasting error,  $\mathcal{D}_{test}(t)$ , on unseen test data, shown in Fig. 4.

From Fig. 4, models whose autoencoder is trained on  $L^2$  loss is better than  $L^1$  loss. Similarly, mean values of relative  $L^1$  and  $L^2$  are a better choice for autoencoder loss,  $\mathcal{L}_{ae}$ , than the mean of  $L^1$  and  $L^2$ , respectively. In general, all the models perform well consistently.

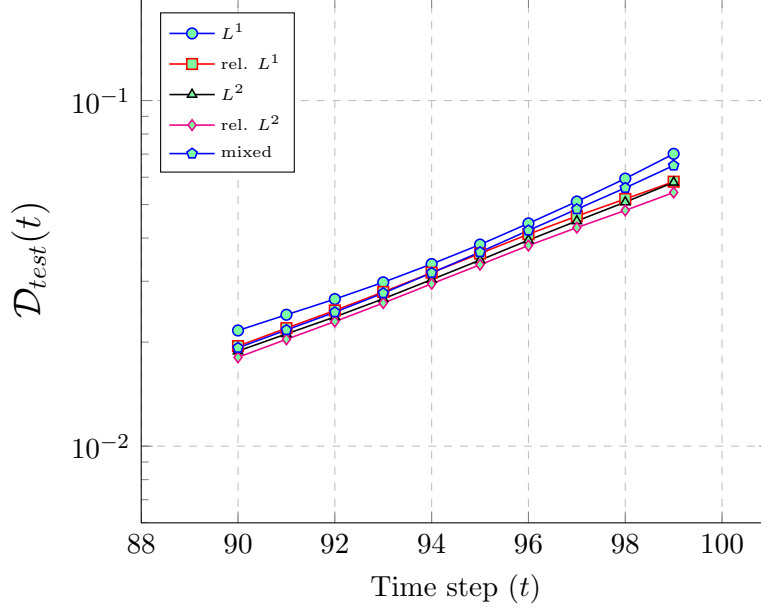


Figure 4: Variation of forecasting error on test data for models with different autoencoder loss functions,  $\mathcal{L}_{ae}$ , specifically  $L^1$ , relative  $L^1$ ,  $L^2$ , relative  $L^2$  and mixed loss ( $L^2$  loss for the initial 5000 epochs and  $L^1$  loss for the remaining epochs).  $\mathcal{D}_{test}(t)$ : represents  $\mathcal{D}(t)$  computed on test dataset as defined by Equation (7).

### 3.2. Performance accuracy and forecasting ability

A representative case for the microstructure evolution at three different time steps is shown in Fig. 5. At the initial time steps, the microstructure is rich with multiple features and evolves rapidly with respect to time. Our surrogate, DeepONet model is able to successfully predict the larger features and the overall morphology of the microstructure. The point-wise error snapshots suggests that the model (1) fails to identify the relatively smaller features in the microstructure, and (2) predictions contains significant errors along the sharp boundaries. In other words, the spatial gradient of the phase concentration is not as sharp as that of the true microstructure from the high-fidelity phase-field simulations.

From Fig. 5, we qualitatively get the intuition that predicted microstructures contain errors at the earlier time steps because of the missing features and at the later time steps due to smoother boundaries predicted by the model. To confirm and quantify this notion, we computed the  $L^2$  norm of relative error at each time step. The  $L^2$  norm of relative error at each time step is defined as:

$$\mathcal{D}(t) = \frac{\sum_x \sum_y \left( \phi(x, y, t) - \hat{\phi}(x, y, t; \theta) \right)^2}{\sum_x \sum_y \phi(x, y, t)^2}, \quad (7)$$

where  $t = 10, 11, \dots, 99$ . To analyze the accuracy of the prediction at each time step, we calculated  $\mathcal{D}(t)$  across the samples in the train and the test datasets, and created a boxplot as shown in Fig. 6. The error is high at the initial time steps, where features are rich and evolve rapidly with time. But the predictions improve over time when the evolution process slows down. The time steps shown in Fig. 6(a) were used during the training of the model. Next, we evaluated the capability of the model to forecast in time at  $t = 90, 91, \dots, 99$ . From

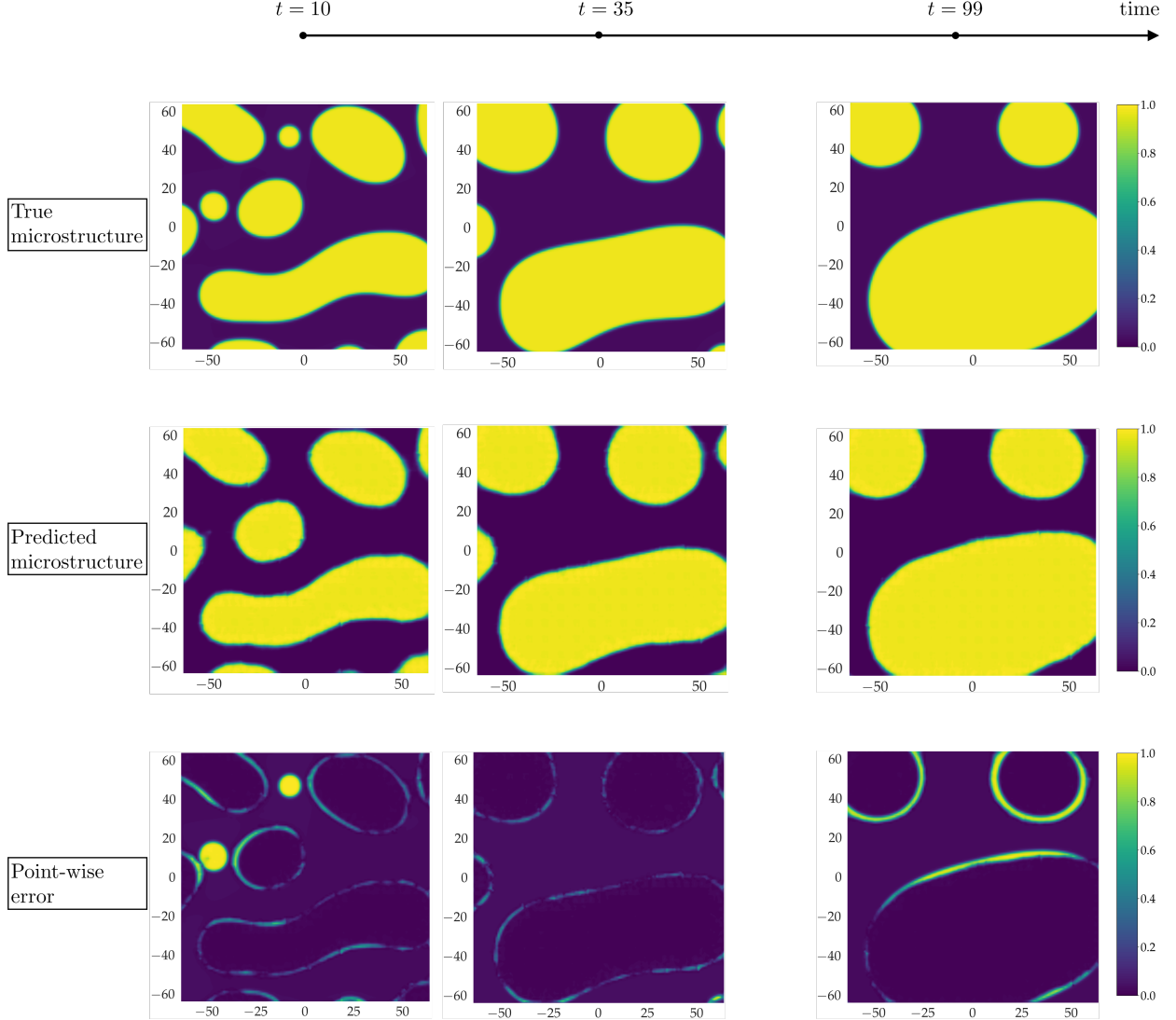


Figure 5: The true, predicted and point-wise error for a microstructure realization evolving in time. The snapshots at time steps  $t = 10, 30, 99$  are shown here. The network used for this simulation has  $l_d = 196$ , and uses the following network architecture. Branch network:  $2 \times [\text{conv}(128, (3, 3))] + [3920]$ . Trunk network:  $2 \times [100] + [3920]$ . The first row presents the ground truth obtained from the high-fidelity phase-field solver MEMPHIS.

Fig. 6(b), error is seen to increase gradually when the model extrapolates at unseen time instances.

A closer look at the forecasting predictions offers further insights on the DeepONet predictive performance. We computed the mean of  $\mathcal{D}(t)$  across the training and the testing datasets for all the models given in Table 2 and plotted these values in Fig. 7. We observe that the mean relative  $L^2$  error reduces by increasing the latent dimension of the autoencoder model. In other words, the model with larger latent spaces is able to predict microstructures better while forecasting. This is intuitive because a larger dimension of the latent space implies that there are more basis functions to express the encoded information about the microstructure and its evolution, and therefore the network has an improved



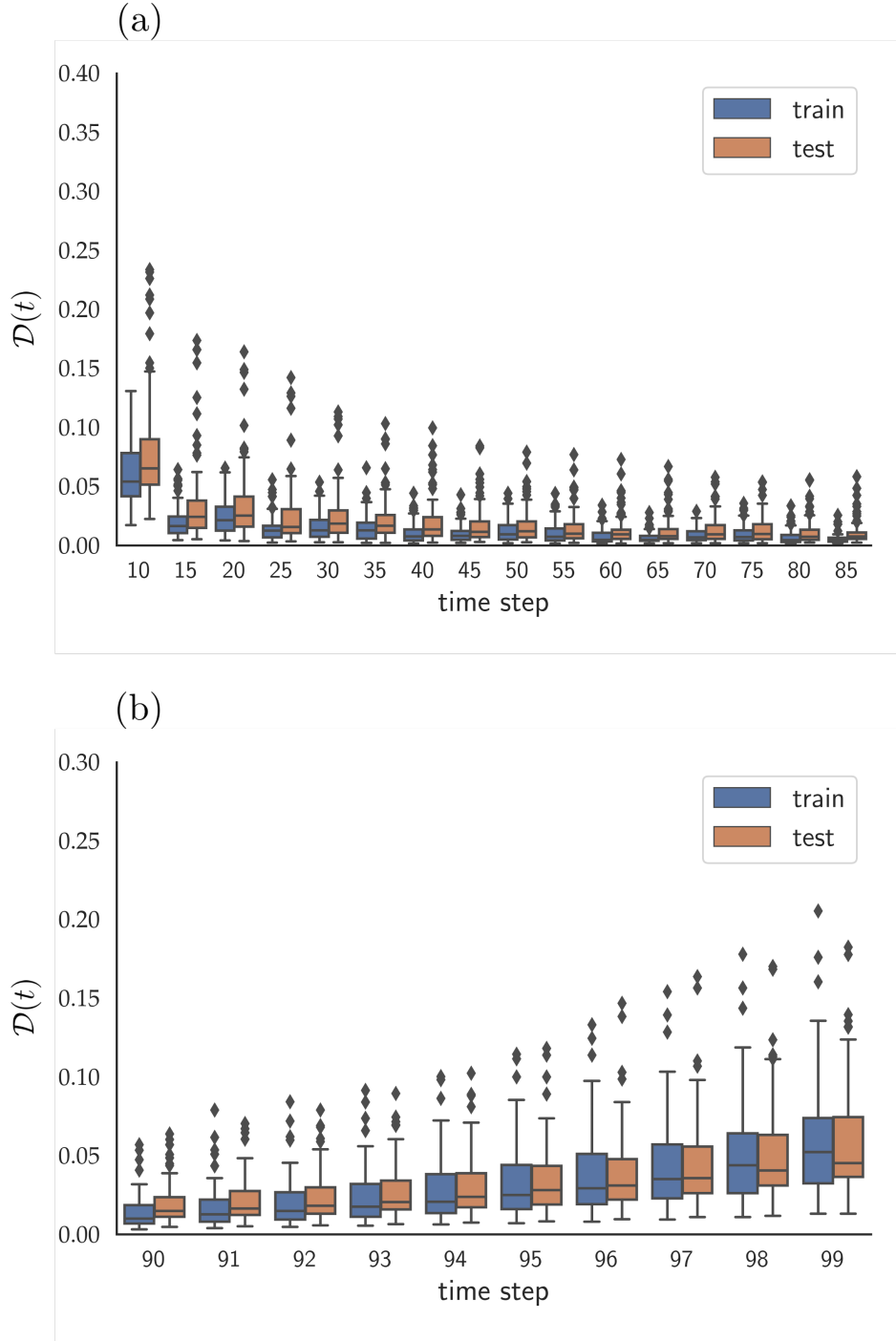


Figure 6: (a) Box plot with respect to  $\mathcal{D}(t)$  computed over the training time steps over the train and test datasets. (b) Same error metric, but in future time steps never seen during the training phase

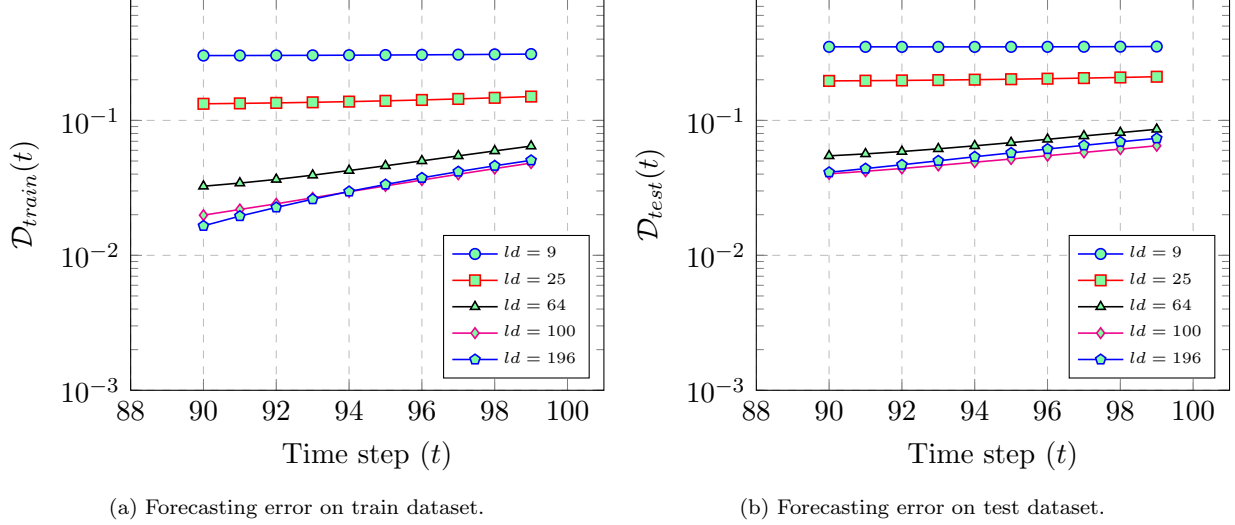


Figure 7: Relative  $L^2$  error for predictions with the train and the test dataset.  $\mathcal{D}_{train}(t)$ ,  $\mathcal{D}_{test}(t)$  represents the mean of  $\mathcal{D}(t)$  computed on train and test datasets respectively, as defined by Equation (7).

% Noise level	$\mathcal{D}_{test}$
0.5	0.04344
1	0.04314
2	0.04260
3	0.04282
4	0.04300
5	0.04364
10	0.04738

Table 3: Prediction errors with noisy inputs

representation capability. However, this trend seems to saturate beyond  $l_d = 100$ . For the model with  $l_d = 100, 196$ , the forecasting error is always less than 6%. The logarithm of the relative  $L^2$ - error linearly increases for  $l_d = 64, 100$  and  $196$  for forecasting time step, whereas for  $l_d = 9$  and  $ld = 25$ , the error is high and remains constant.

### 3.3. Robustness of the surrogate DeepONet framework: Sensitivity to noise

We investigated how the accuracy of prediction varies by systematically increasing the noise levels in the model input. For this analysis, we considered the best model with  $l_d = 196$  and DeepONet architecture 1 (see Table 2) with sin activation functions. We added a Gaussian white noise with mean zero and standard deviations,  $\sigma = 0.5\%, 1\%, 2\%, 3\%, 4\%, 5\%, 10\%$ . To evaluate the model performance, we used the relative  $L^2$  norm,  $\mathcal{D}$ , as defined in equation 6.  $\mathcal{D}$  is calculated across the samples present in the test dataset.

From Table 3 and Fig. 8, the relative  $L^2$  norm does not increase much when noise is added to the model input. Previous studies [46–48] illustrated the capability of the

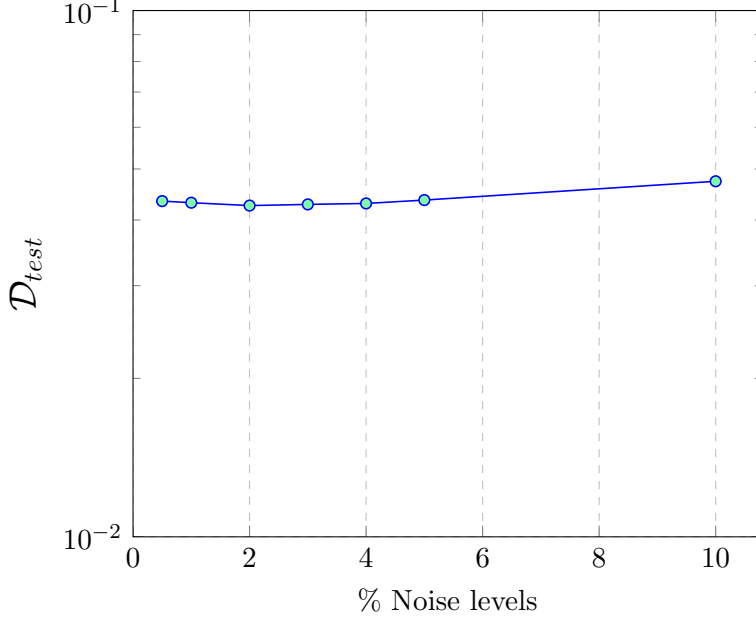


Figure 8: Sensitivity of the proposed surrogate model to different levels of noise added to the test data.  $\mathcal{D}_{test}$ : represents the mean of  $\mathcal{D}$  computed on test dataset as defined by Equation (6).

autoencoders to denoise noisy images. The transformation to a low-dimensional latent space forces the autoencoders to retain the dominant features alone. The convolutional autoencoder used in this approach does exactly that by de-noising the noisy microstructure input. The output of the convolutional encoder is almost in its pure form, free from noise and therefore enables the DeepONet to make stable predictions. The decoder accurately reconstructs the microstructure from the predictions made by DeepONet in the latent space.

#### 3.4. Training strategy for learning small scale features

It is to be noted that the present DeepONet model is not able to capture the small scale microstructure features as shown in Figure 5. During the evolution of the system, the small scale features coalesce to form the larger regions of similar phases and therefore the surrogate model approximates the microstructure fairly well at the later time steps as shown earlier. Figure 6 also quantifies the difficulty of the proposed framework to model microstructure evolution at the earlier timesteps.

To circumvent this issue, during training of the DeepONet model, we increased the weight given to earlier time steps of each realization in the dataset. In particular, we forced the DeepONet model,  $\mathcal{G}(\tilde{\Phi})(t; \theta_d)$ , to predict earlier time steps repeatedly and subsequently, we endowed training dataset with repeated  $\tilde{\phi}(t)$  for each realization. Since the DeepONet model is trained to minimize the mean squared error between these two terms, the model is driven to give greater emphasis to earlier time steps. The results from this training procedure are depicted in Figure 9.

From Figure 9, we observe that increasing the weight given to the earlier time steps of evolution for each realization results in a DeepONet model capable of recovering finer, high frequency components.

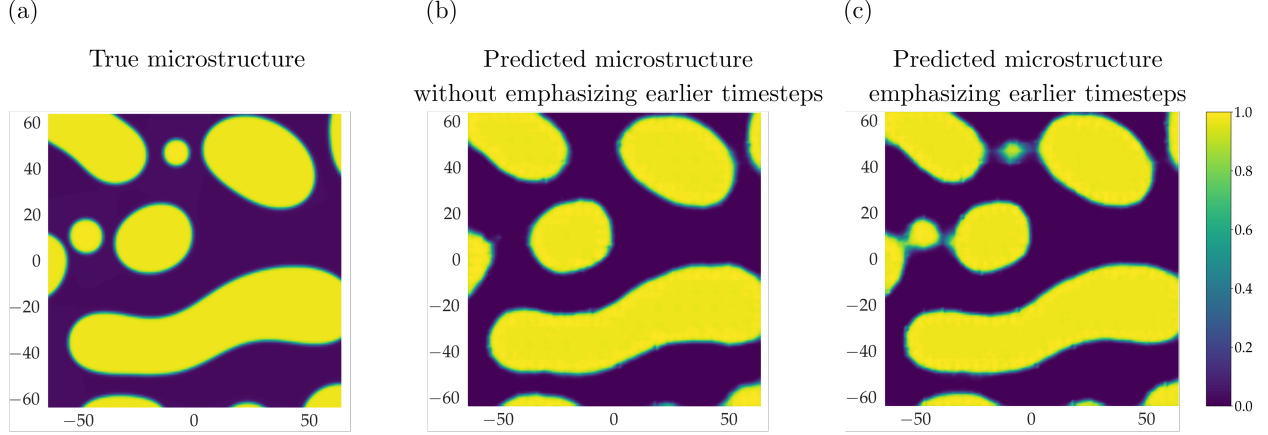


Figure 9: (a) True microstructure at  $t = 10$ . (b) Predicted microstructure without emphasizing earlier time steps during training. (c) Microstructure predicted by DeepONet trained on a dataset where the earlier timesteps were repeated to increase the importance given to earlier timesteps.

#### 4. Summary and Discussion

In this work, we investigated the effectiveness of the proposed convolutional autoencoder–DeepONet approach for modeling the evolution dynamics of mesoscale microstructures. We trained our model on high-fidelity, phase-field data generated by solving the Cahn-Hilliard equation. We performed a series of analyses to (1) investigate the effect of the dimension of the latent space learned by the convolutional autoencoder, (2) analyze the capability of the proposed approach to extrapolate in time by forecasting beyond the training steps, and (3) observe how the trained model responds to noisy inputs. The primary advantages of the convolutional autoencoder–DeepONet approach are listed below:

- Unlike the existing methods that train machine-learning-based surrogate models using low-dimensional representations of autocorrelations of microstructures, this model learns a suitable low-dimensional latent space using a convolutional autoencoder. As the next step, the surrogate model learns the underlying operator responsible for the evolution of microstructure using DeepONet in the latent space. The learned latent variables are fed to the pretrained decoder to reconstruct the microstructure. We note that this approach bypasses any postprocessing steps such as a phase-recovery algorithm necessary to reconstruct the microstructure from statistical functions [35].
- Although we have trained our autoencoder model, we believe that any autoencoder finely trained on image datasets will be suitable for this task. Reusing such pre-trained autoencoders readily available can greatly save computational cost.
- The advantage of training DeepONet in low-dimensional latent space is two-fold. Firstly, training DeepONet in a low-dimensional space is computationally efficient. Secondly, the presence of several high gradient regions in the microstructure data (see Fig. 10 (a)) makes it challenging to train a neural network. The encoder transforms microstructure data to a latent space (Fig. 10(b)), where the gradients are not high.

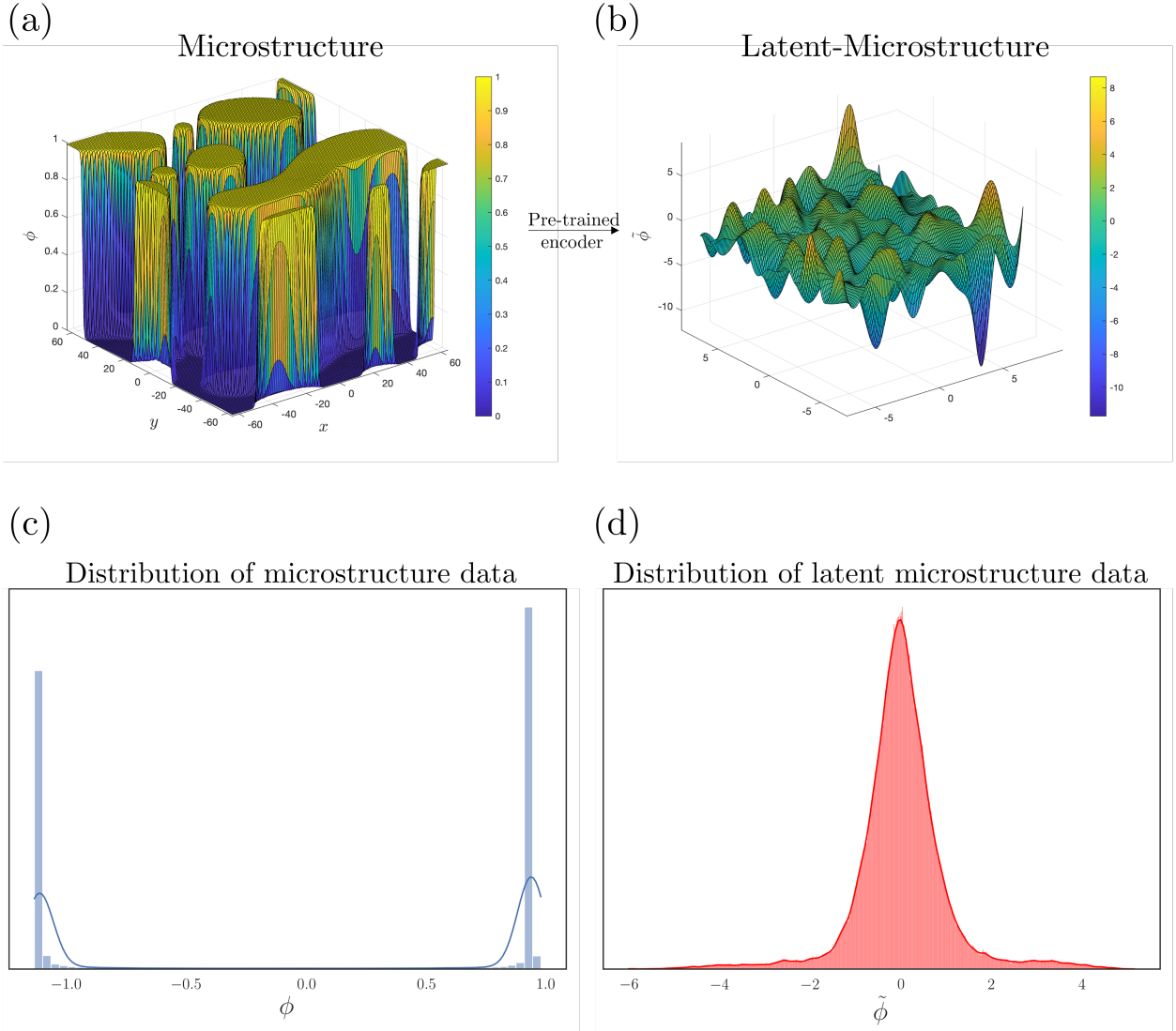


Figure 10: (a) 3D visualization of the function to be approximated by the surrogate model. The presence of several high-gradient regions at every time-step, makes it challenging for neural network models to learn the evolution dynamics of microstructures. (b) A smoother latent-microstructure learned by the encoder during the autoencoder training. (c) The microstructure data,  $\phi(x, y, t)$ , is predominantly 1s or 0s. (d) The encoder transforms  $\phi$  to a latent space,  $\tilde{\phi}$ , where deep neural networks can learn easily. The curves in (c) and (d) represent the smoothed density estimates of the histogram

In other words, the encoder learns a non-linear mapping of the microstructure data coming from an untrainable distribution in the primitive space, as shown in Fig. 10(c) to a more trainable distribution in the low dimensional latent space, as shown in Fig. 10(d).

- The training and inference using DeepONet is much faster than the LSTM network. This is because the fully connected layers in the trunk network and convolutional layers in the branch network of the DeepONet architecture can be parallalized unlike LSTMs, due to lack of temporal dependencies. This makes training and inference of DeepONet significantly faster than the popular recurrent neural network architectures such as LSTMs and GRUs.
- The entire history about the microstructure evolution in latent space, from  $t = 10$  to  $t = 89$ , is fed to branch network. DeepONet successfully extrapolates in time beyond the training time steps, providing accurate forecasting results for the next 10 time steps while keeping the relative  $L^2$  error under 5% for both train dataset and never seen before test datasets.
- The proposed method is quite robust to noisy inputs. The de-noising nature of a trained autoencoder enables the encoder to learn a stable and consistent mapping to the latent space. The encoder filters out noise and only retains the dominant eigen components of the microstructure data. This makes training of the DeepONet to learn the growth dynamics in the latent space much more stable in predicting the microstructure at any desired time step accurately. The approach is almost invariant to noise up to 10% Gaussian white noise, as presented in Table 3 and Fig. 8.
- We perform computational experiments to investigate the sensitivity of model to (1) number of training data samples, and (2) the choice of loss function used for traning of the autoencoder. The model achieves good prediction accuracy on test dataset, with only 1200 training samples and is not sensitive to the choice of the loss functions.

## Acknowledgements

RD and GEK acknowledge funding under the *BeyondFingerprinting* Sandia Grand Challenge Laboratory Directed Research and Development (GC LDRD) program. The phase-field framework is supported by the Center for Integrated Nanotechnologies (CINT), an Office of Science user facility operated for the U.S. Department of Energy. This research was conducted using computational resources and services at the Center for Computation and Visualization, Brown University. Sandia National Laboratories is a multi-mission laboratory managed and operated by National Technology and Engineering Solutions of Sandia, LLC., a wholly owned subsidiary of Honeywell International, Inc., for the U.S. Department of Energy National Nuclear Security Administration under contract DE-NA0003525. This paper describes objective technical results and analysis. Any subjective views or opinions that might be expressed in the paper do not necessarily represent the views of the U.S. Department of Energy or the United States Government.

## References

- [1] L.-Q. Chen, Phase-Field Models for Microstructure Evolution, *Annual Review of Materials Research* 32 (1) (2002) 113–140.
- [2] N. Moelans, B. Blanpain, P. Wollants, An introduction to phase-field modeling of microstructure evolution, *Calphad* 32 (2) (2008) 268–294.
- [3] Z. Yang, C.-H. Yu, M. J. Buehler, Deep learning model to predict complex stress and strain fields in hierarchical composites, *Science Advances* 7 (15) (2021) eabd7416.
- [4] R. Pokharel, A. Pandey, A. Scheinker, Physics-Informed Data-Driven Surrogate Modeling for Full-Field 3D Microstructure and Micromechanical Field Evolution of Polycrystalline Materials, *JOM* 73 (11) (2021) 3371–3382.
- [5] S. Chakraborty, S. Goswami, T. Rabczuk, A surrogate assisted adaptive framework for robust topology optimization, *Computer Methods in Applied Mechanics and Engineering* 346 (2019) 63–84.
- [6] E. Olsson, G. Kreiss, A conservative level set method for two phase flow, *Journal of Computational Physics* 210 (1) (2005) 225–246.
- [7] P. Yue, C. Zhou, J. J. Feng, C. F. Ollivier-Gooch, H. H. Hu, Phase-field simulations of interfacial dynamics in viscoelastic fluids using finite elements with adaptive meshing, *Journal of Computational Physics* 219 (1) (2006) 47–67.
- [8] R. Bharali, S. Goswami, C. Anitescu, T. Rabczuk, A robust monolithic solver for phase-field fracture integrated with fracture energy based arc-length method and under-relaxation, *arXiv preprint arXiv:2111.10649* (2021).
- [9] S. Goswami, C. Anitescu, T. Rabczuk, Adaptive fourth-order phase field analysis for brittle fracture, *Computer Methods in Applied Mechanics and Engineering* 361 (2020) 112808.
- [10] J. A. Stewart, R. Dingreville, Microstructure morphology and concentration modulation of nanocomposite thin-films during simulated physical vapor deposition, *Acta Materialia* 188 (2020) 181–191.
- [11] M. Powers, J. A. Stewart, R. Dingreville, B. K. Derby, A. Misra, Compositionally-driven formation mechanism of hierarchical morphologies in co-deposited immiscible alloy thin films, *Nanomaterials* 11 (10) (2021) 2635.
- [12] I. Beyerlein, A. Hunter, Understanding dislocation mechanics at the mesoscale using phase field dislocation dynamics, *Philosophical Transactions of the Royal Society A: Mathematical, Physical and Engineering Sciences* 374 (2066) (2016) 20150166.
- [13] C. M. Elliott, D. A. French, Numerical studies of the Cahn-Hilliard equation for phase separation, *IMA Journal of Applied Mathematics* 38 (2) (1987) 97–128.

- [14] J. W. Cahn, J. E. Hilliard, Free Energy of a Nonuniform System. I. Interfacial Free Energy, *The Journal of Chemical Physics* 28 (2) (1958) 258–267.
- [15] Z. Z. Sun, A second-order accurate linearized difference scheme for the two-dimensional Cahn-Hilliard equation, *Mathematics of Computation* 64 (212) (1995) 1463–1471.
- [16] C. Liu, J. Shen, A phase field model for the mixture of two incompressible fluids and its approximation by a Fourier-spectral method, *Physica D: Nonlinear Phenomena* 179 (3-4) (2003) 211–228.
- [17] J. W. Barrett, J. F. Blowey, H. Garcke, Finite element approximation of the Cahn-Hilliard equation with degenerate mobility, *SIAM Journal on Numerical Analysis* 37 (1) (1999) 286–318.
- [18] H. Gómez, V. M. Calo, Y. Bazilevs, T. J. Hughes, Isogeometric analysis of the Cahn-Hilliard phase-field model, *Computer Methods in Applied Mechanics and Engineering* 197 (49-50) (2008) 4333–4352.
- [19] C. L. Chan, C. Anitescu, T. Rabczuk, Strong multipatch C1-coupling for isogeometric analysis on 2D and 3D domains, *Computer Methods in Applied Mechanics and Engineering* 357 (2019) 112599.
- [20] N. D. Alikakos, P. W. Bates, X. Chen, Convergence of the Cahn-Hilliard equation to the Hele-Shaw model, *Archive for Rational Mechanics and Analysis* 128 (2) (1994) 165–205.
- [21] D. B. Brough, A. Kannan, B. Haaland, D. G. Bucknall, S. R. Kalidindi, Extraction of process-structure evolution linkages from x-ray scattering measurements using dimensionality reduction and time series analysis, *Integrating materials and manufacturing innovation* 6 (2) (2017) 147–159.
- [22] S. Pfeifer, O. Wodo, B. Ganapathysubramanian, An optimization approach to identify processing pathways for achieving tailored thin film morphologies, *Computational Materials Science* 143 (2018) 486–496.
- [23] G. H. Teichert, K. Garikipati, Machine learning materials physics: Surrogate optimization and multi-fidelity algorithms predict precipitate morphology in an alternative to phase field dynamics, *Computer Methods in Applied Mechanics and Engineering* 344 (2019) 666–693.
- [24] C. Lin, M. Maxey, Z. Li, G. E. Karniadakis, A seamless multiscale operator neural network for inferring bubble dynamics, *Journal of Fluid Mechanics* 929 (2021).
- [25] S. Goswami, M. Yin, Y. Yu, G. Karniadakis, A physics-informed variational DeepONet for predicting the crack path in brittle materials, *arXiv preprint arXiv:2108.06905* (2021).
- [26] Z. Li, N. Kovachki, K. Azizzadenesheli, B. Liu, K. Bhattacharya, A. Stuart, A. Anandkumar, Fourier Neural Operator for Parametric Partial Differential Equations, *arXiv preprint arXiv:2010.08895* (2020).



- [27] S. Goswami, C. Anitescu, S. Chakraborty, T. Rabczuk, Transfer learning enhanced physics informed neural network for phase-field modeling of fracture, *Theoretical and Applied Fracture Mechanics* 106 (2020) 102447.
- [28] E. Haghighat, M. Raissi, A. Moure, H. Gomez, R. Juanes, A physics-informed deep learning framework for inversion and surrogate modeling in solid mechanics, *Computer Methods in Applied Mechanics and Engineering* 379 (2021) 113741.
- [29] S. Goswami, C. Anitescu, T. Rabczuk, Adaptive fourth-order phase field analysis using deep energy minimization, *Theoretical and Applied Fracture Mechanics* 107 (2020) 102527.
- [30] E. Samaniego, C. Anitescu, S. Goswami, V. M. Nguyen-Thanh, H. Guo, K. Hamdia, X. Zhuang, T. Rabczuk, An energy approach to the solution of partial differential equations in computational mechanics via machine learning: Concepts, implementation and applications, *Computer Methods in Applied Mechanics and Engineering* 362 (2020) 112790.
- [31] K. Shukla, A. D. Jagtap, J. L. Blackshire, D. Sparkman, G. E. Karniadakis, A Physics-Informed Neural Network for Quantifying the Microstructural Properties of Polycrystalline Nickel Using Ultrasound Data: A promising approach for solving inverse problems, *IEEE Signal Processing Magazine* 39 (1) (2022) 68–77.
- [32] D. M. de Oca Zapiain, J. A. Stewart, R. Dingreville, Accelerating phase-field-based microstructure evolution predictions via surrogate models trained by machine learning methods, *npj Computational Materials* 7 (1) (2021) 1–11.
- [33] C. Hu, S. Martin, R. Dingreville, Accelerating phase-field predictions via recurrent neural networks learning the microstructure evolution in latent space, *Computer Methods in Applied Mechanics and Engineering* (2022) accepted.
- [34] D. T. Fullwood, S. R. Niezgoda, S. R. Kalidindi, Microstructure reconstructions from 2-point statistics using phase-recovery algorithms, *Acta Materialia* 56 (5) (2008) 942–948.
- [35] E. Herman, J. A. Stewart, R. Dingreville, A data-driven surrogate model to rapidly predict microstructure morphology during physical vapor deposition, *Applied Mathematical Modelling* 88 (2020) 589–603.
- [36] L. Lu, P. Jin, G. Pang, Z. Zhang, G. E. Karniadakis, Learning nonlinear operators via DeepONet based on the universal approximation theorem of operators, *Nature Machine Intelligence* 3 (3) (2021) 218–229.
- [37] C. Lin, Z. Li, L. Lu, S. Cai, M. Maxey, G. E. Karniadakis, Operator learning for predicting multiscale bubble growth dynamics, *The Journal of Chemical Physics* 154 (10) (2021) 104118.

- [38] R. P. M. Dingreville, J. A. Stewart, E. Y. Chen, J. M. Monti, Benchmark problems for the Mesoscale Multiphysics Phase Field Simulator (MEMPHIS), Tech. rep., Sandia National Laboratories, Albuquerque, NM (United States) (2020).
- [39] E. Süli, D. F. Mayers, An Introduction to Numerical Analysis, Cambridge University Press, 2003.
- [40] S. R. Niezgoda, A. K. Kanjarla, S. R. Kalidindi, Novel microstructure quantification framework for databasing, visualization, and analysis of microstructure data, *Integrating Materials and Manufacturing Innovation* 2 (1) (2013) 54–80.
- [41] A. Gupta, A. Cecen, S. Goyal, A. K. Singh, S. R. Kalidindi, Structure–property linkages using a data science approach: application to a non-metallic inclusion/steel composite system, *Acta Materialia* 91 (2015) 239–254.
- [42] K. Lee, K. T. Carlberg, Model reduction of dynamical systems on nonlinear manifolds using deep convolutional autoencoders, *Journal of Computational Physics* 404 (2020) 108973.
- [43] D. P. Kingma, J. Ba, Adam: A Method for Stochastic Optimization, arXiv preprint arXiv:1412.6980 (2014).
- [44] M. Abadi, A. Agarwal, P. Barham, E. Brevdo, Z. Chen, C. Citro, G. S. Corrado, A. Davis, J. Dean, M. Devin, et al., TensorFlow: Large-Scale Machine Learning on Heterogeneous Distributed Systems, Software available from [tensorflow.org](https://www.tensorflow.org). 1 (2) (2015).
- [45] X. Glorot, Y. Bengio, Understanding the difficulty of training deep feedforward neural networks, in: *Proceedings of the Thirteenth International Conference on Artificial Intelligence and Statistics*, 2010, pp. 249–256.
- [46] P. Vincent, H. Larochelle, Y. Bengio, P.-A. Manzagol, Extracting and Composing Robust Features with Denoising Autoencoders, in: *Proceedings of the 25th International Conference on Machine Learning*, 2008, pp. 1096–1103.
- [47] P. Vincent, H. Larochelle, I. Lajoie, Y. Bengio, P.-A. Manzagol, L. Bottou, Stacked Denoising Autoencoders: Learning Useful Representations in a Deep Network with a Local Denoising Criterion, *Journal of Machine Learning Research* 11 (12) (2010).
- [48] L. Gondara, Medical Image Denoising Using Convolutional Denoising Autoencoders, in: *2016 IEEE 16<sup>th</sup> International Conference on Data Mining Workshops (ICDMW)*, IEEE, 2016, pp. 241–246.